Torque Ripple Suppression in Three-Phase Doubly-Fed Machine for Wireless Power Transfer in Integrated Drives

Torque Ripple Suppression in Three-Phase Doubly-Fed Machine for Wireless Power Transfer in Integrated Drives

G. Rizzoli, M. Mengoni, *Member, IEEE,* L. Vancini, G. Sala, *Member, IEEE,*
L. Zarri, *Senior Member, IEEE,* and A. Tani

Abstract—**Rotary assembly platforms are commonly used in the packaging industry. One of the problems that the designers have to solve is how to transfer power to auxiliary actuators mounted on a rotating disk. The preferred solution is to avoid sliding contacts to improve the system reliability and minimize maintenance costs. To achieve this result, a three-phase doubly-fed induction machine can be used to independently control the motion of the rotating disk and the power delivered to the rotating loads of the platform. In any operating condition, the independent control of the power transfer and the torque can be achieved by adding a pulsating component to the machine flux. This paper focuses on the analysis and minimization of the torque contributions generated by the machine due to the interaction between the low and high frequency of the flux contributions. Experimental results confirm the feasibility of the proposed solution to improve the torque quality and the accuracy of the drive.**

Index Terms— **Position control, wireless power transfer, induction motors, machine vector control, variable speed drives.**

NOMENCLATURE

$\bar{v}_S, \bar{v}_R$	Space vectors of the stator and rotor voltages in the d-q reference frame.
$\bar{\imath}_S, \bar{\imath}_R$	Space vectors of the stator and rotor currents in the d-q reference frame.
$\bar{\varphi}_S, \bar{\varphi}_R$	Space vectors of the stator and rotor flux linkage in the d-q reference frame.
$\bar{y}_L, \bar{y}_H$	Low-frequency and High-frequency decomposition of the generic variable $\bar{y}$ (current, voltages and fluxes).
y_{Ld}, y_{Lq}	d-q components of the generic variable $\bar{y}_L$.
y_{Hd}, y_{Hq}	d-q components of the generic variable $\bar{y}_H$.
Y_{Hd}, Y_{Hq}	Modules of the sinusoidal variables y_{Hd} and y_{Hq}.
γ_{Hd}, γ_{Hq}	Angle of the sinusoidal variables y_{Hd} and y_{Hq}.
ω_H	Angular frequency of the sinusoidal high frequency variables.
ω_m	Shaft speed in electrical radians per second.
ω	Generic speed of the d-q reference frame.
ω_L	Angular speed of the low frequency contribution of the rotor flux.
ϑ_L	Angle of the low frequency rotor flux, used for the d-q Park transformation.
T	Total torque at the shaft.
T_L	Torque contribution due to the interaction between low frequency stator and rotor variables $\bar{y}_L$.
T_{LH}	Torque generated by the interaction between low and high frequency stator and rotor variables $\bar{y}_L$ and $\bar{y}_H$.
T_H	Torque contribution due to the interaction between high frequency stator and rotor variables $\bar{y}_H$.
$T_{H,DC}$	Average value of T_H.
$T_{H,AC}$	AC term of torque T_H.
P_R	Total power extracted from the rotor windings.
$\hat{P}_R$	Average power extracted from the rotor windings.
$P_{R,L}$	Power contribution due to the interaction between low frequency stator and rotor variables $\bar{y}_L$.
$P_{R,LH}$	Power contribution due to the interaction between low and high frequency stator and rotor variables.
$P_{R,H}$	Power contribution due to the interaction between high frequency stator and rotor variables $\bar{y}_H$.
P_{LOAD}	Power absorbed by the rotor loads.
V_{exc}	Excitation voltage that is induced on the rotor windings due to the pulsating current i_{SHd}.
R_{VR}	Virtual resistance of the rotor load, used to control the power $\hat{P}_{R,Ld}$.
E_{DCS}	DC-link voltage of the stator inverter.
E_{DCR}	DC-link voltage of the rotor inverter.

I. INTRODUCTION

ROTARY assembly tables are machines commonly used in the packaging industry to perform automated tasks such as bottle filling and capping. A practical example of these systems is the device shown in Fig. 1. The core of the platform consists of a rotating positioning disk on which the objects that must undergo a machining process are placed. As the platform rotates, each object completes one revolution around the disk's axis and goes through some sequential processing stations. In modern platforms, actuators and sensors are positioned on the

Gabriele Rizzoli, Michele Mengoni, Luca Vancini, Giacomo Sala, Luca Zarri and Angelo Tani are with the Department of Electrical, Electronic and Information Engineering "Guglielmo Marconi", University of Bologna, Bologna, 40136, Italy (gabriele.rizzoli@unibo.it, michele.mengoni@unibo.it, luca.vancini4@unibo.it, g.sala@unibo.it, luca.zarri2@unibo.it, angelo.tani@unibo.it).

Fig. 1. - Example of rotary assembly station.

Fig. 2. Conceptual representation of the integrated drive for rotary assembly stations.
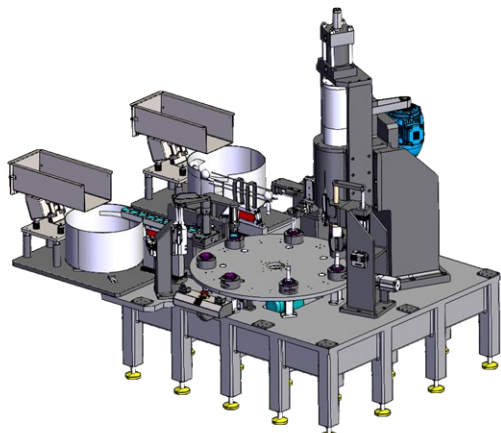
rotating plate to enhance the functionality of the process. These sensors include electric actuators, cutters, position probes, process cameras, temperature probes, industrial controllers, antennas, and small compressors for pneumatic actuators. Therefore, a system that transfers energy from the fixed frame to the rotating one is required. The approach usually adopted by the industry is to transfer energy and control signals to the rotating platform through slip rings consisting of electrical brushes that rub on a conductive ring. However, sliding contacts are subject to wear and require frequent maintenance and preventive replacement to ensure the high reliability of the production line [1]-[5]. Consequently, rotating transformers [6]-[11] and capacitively coupled systems [12]-[13] have been proposed as effective alternatives to slip-rings, allowing the contactless transmission of power to the rotating loads.

A different approach to address the problem is to use a drive that integrates Wireless Power Transfer (WPT) and propulsion capabilities. Such a system must provide the independent control of torque and the rotor power in any operating condition.

One possible way to implement a system with these characteristics is to use mixed-pole wound-rotor machines [14]. This type of electromagnetic structure has two distinct three-phase windings with different numbers of pole pairs on both the stator and the rotor. This technique allows the independent control of two spatial harmonics of the air gap magnetic flux [15], allowing the independent control of the torque and rotor power transfer. This machine is a combination of an electric motor and a rotary transformer.

Among the possible solutions, the most innovative approach consists in an integrated drive based on a wound-rotor five-phase induction machine [16]-[17]. The degrees of freedom in the control of the five-phase machine allow the fundamental component of the magnetic field in the airgap to be used for torque generation and the third harmonic component for WPT purposes. The benefit of this approach is that the torque generated by the machine shows a negligible ripple and is not affected by the power transfer. Nevertheless, using five-phase inverters and a wound-rotor five-phase induction machine can be considered a limiting factor in an industrial sector dedicated to three-phase solutions.
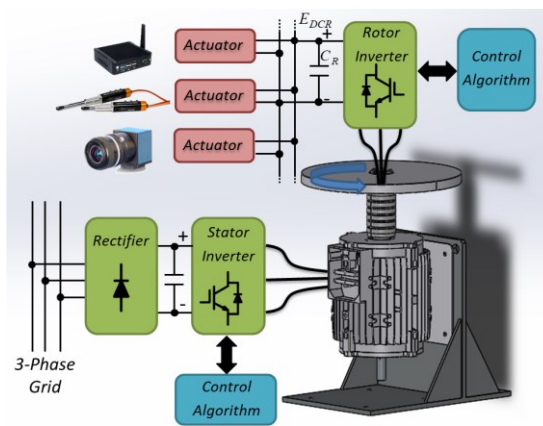
A more standard three-phase Doubly-Fed Induction Machines (DF-IM) can be used to fulfill the requirements of rotary positioning systems. However, decoupling the power transfer and the torque generation is more difficult with respect to multiphase solutions. Three-phase DF-IM find their main application as generators in wind turbines, where they can adapt to the fluctuating wind speed and optimize the output power by injecting/absorbing power from both the rotor and stator windings [18]-[20]. Therefore, this type of machine and its control scheme seem to be suitable for rotary assembly stations, where the control of the motion and the rotor power are required. However, in wind turbines, the stator winding of the DF-IM is directly connected to the grid, while the rotor is fed through a back-to-back inverter. This configuration minimizes the cost and weight of power converters at the expense of a limited rotor speed range variation and the coupling between the torque reference and the rotor power. Thus, the standard control scheme for DF-IM does not meet the requirements of the rotary assembly station. A control scheme that allows the separate control of torque and rotor power is the Single External Feeding (SEF) for DF-IMs [21]. In this solution, the rotor inverter is located on the rotor and absorbs only the power required by the rotor side loads (inverter losses, control system, sensors, etc.) at the expense of the coupling between the active and reactive power injected into the grid. However, this scheme fails to control the rotor power when the torque demand is zero, or the machine is close to the synchronous speed. Both conditions rarely occur in DF-IM for wind turbines, while the same control scheme used for variable speed drives is more likely to face these events. Therefore, to control the power flow in any operating condition, including standstill and zero torque, electromotive forces should be induced in the rotor windings as in a transformer by adding pulsating terms in the machine currents and flux linkages [22]. The drawback of this approach is that the interaction between the low-frequency and high-frequency currents of the machine generally produces a pulsating torque, which reduces the performance and the accuracy of the drive. To mitigate this problem, the control algorithm can be modified to reduce the torque ripple by orienting the high-frequency current vector in the same direction as the rotor flux [23]. However, the method cannot

entirly cancel the torque pulsation. The ripple is only shifted to a higher frequency where the inertia of the system helps filter the vibrations generated by the drive.

This paper extends the proof-of-concept presented in [23] and introduces new features that are crucial in practical industrial applications. The main contributions of this work are briefly illustrated hereafter:

- the analysis of the torque ripple components generated by the interaction between low-frequency and high-frequency current is presented in detail;
- the concept of virtual load resistance is introduced to modulate and control the amount of power transferred to the rotating loads;
- the proposed control scheme completely suppresses the torque ripple generated by the simultaneous control of the motion and the power transferred to the rotor.

The remaining part of this paper is organized as follows. The mathematical analysis of Section II is used to derive the conditions for the suppression of the torque ripple generated by the machine, and a suitable control scheme is presented in Section III. The experimental results reported in Section IV confirm the theoretical analysis and demonstrate the feasibility of the proposed solution.

II. DESCRIPTION OF THE SYSTEM

The conceptual representation of the integrated drive for rotary assembly platforms is shown in Fig. 2. The core of the system is a gearless three-phase doubly-fed induction machine. The stator winding is fed by the stator inverter, while the rotor winding is connected to an inverter mounted on the rotating platform. The rotor inverter operates as a PWM active rectifier to generate the constant DC voltage necessary to power the actuators and sensors located on the rotating disk.

A. Mathematical model of the drive

The dynamic behavior of the wound-rotor induction machine can be represented by the following equations written in a generic d-q reference frame:

$$\bar{v}_S = R_S \bar{i}_S + \frac{d\bar{\varphi}_S}{dt} + j\omega\bar{\varphi}_S \tag{1}$$

$$\bar{v}_R = R_R \bar{i}_R + \frac{d\bar{\varphi}_R}{dt} + j(\omega - \omega_m)\bar{\varphi}_R \tag{2}$$

$$\bar{\varphi}_S = L_S \bar{i}_S + M \bar{i}_R \tag{3}$$

$$\bar{\varphi}_R = L_R \bar{i}_R + M \bar{i}_S \tag{4}$$

$$T = \frac{3}{2} p \frac{M}{L_R} (j\bar{\varphi}_R) \cdot \bar{i}_S \tag{5}$$

$$P_R = -\frac{3}{2} \bar{v}_R \cdot \bar{i}_R \tag{6}$$

where $\bar{v}_S$ and $\bar{v}_R$ are the stator and rotor voltage vectors, $\bar{i}_S$ and $\bar{i}_R$ are the current vectors, $\bar{\varphi}_S$ and $\bar{\varphi}_R$ are the flux vectors, T is the electromagnetic torque, and P_R is the active power extracted from the machine by the rotor inverter. If P_R is positive, the power flow is from the rotor toward the inverter. Also, R_S and R_R are the stator and rotor resistances, L_S, L_R, and M are the stator, rotor, and mutual inductances, ω is the angular frequency

of the d-q reference frame, ω_m is the speed of the machine in electrical radians per second, and p is the number of pole pairs. The dot operator "·" in (5) and (6) is the product of the magnitude of two vectors and the cosine of the angle between them.

The electric drive behaves like an integrated system that controls the motion and transfers energy to the rotor loads only if the power P_R in (6) and the torque T in (5) can be independently controlled. In the scheme of Fig. 2, the rotor loads are connected to the DC-link capacitor C_R of the rotor inverter. Thus, the power P_R must be adjusted to keep the voltage E_{DCR} constant according to the following equation:

$$\frac{d}{dt}\left(\frac{1}{2}C_R E_{DCR}^2\right) = P_R - P_{LOAD}. \tag{7}$$

At steady state, E_{DCR} is constant, and the power delivered to the auxiliary actuators is equal to that received by the rotor inverter, apart from the inverter losses. A viable method to decouple the torque control from the electric energy transfer is to split the electric vector variables of the machine into Low (L) and High (H) frequency components, as follows:

$$\bar{v}_S = \bar{v}_{SL} + \bar{v}_{SH} \tag{8}$$

$$\bar{i}_S = \bar{i}_{SL} + \bar{i}_{SH} \tag{9}$$

$$\bar{\varphi}_S = \bar{\varphi}_{SL} + \bar{\varphi}_{SH} \tag{10}$$

$$\bar{v}_R = \bar{v}_{RL} + \bar{v}_{RH} \tag{11}$$

$$\bar{i}_R = \bar{i}_{RL} + \bar{i}_{RH} \tag{12}$$

$$\bar{\varphi}_R = \bar{\varphi}_{RL} + \bar{\varphi}_{RH}. \tag{13}$$

Fig. 3 shows an example of frequency decomposition for a general vector quantity $\bar{y}$ into the low-frequency and high-frequency components, respectively, $\bar{y}_L$ and $\bar{y}_H$. The trajectories followed by the two vectors are independent in shape and travel speed.

By replacing (8)-(13) into (1)-(4), it can be noted that low-frequency currents and flux linkages can be controlled by acting on $\bar{v}_{SL}$ and $\bar{v}_{RL}$, while the high-frequency currents and fluxes depend only on $\bar{v}_{SH}$ and $\bar{v}_{RH}$. Therefore, (1)-(4) can be split into two independent set of equations, which represent the electric dynamics of the system due to the low-frequency and high-frequency variables:

$$\bar{v}_{SL} = R_S \bar{i}_{SL} + \frac{d\bar{\varphi}_{SL}}{dt} + j\omega\bar{\varphi}_{SL} \tag{14}$$

$$\bar{v}_{RL} = R_R \bar{i}_{RL} + \frac{d\bar{\varphi}_{RL}}{dt} + j(\omega - \omega_m)\bar{\varphi}_{RL} \tag{15}$$

$$\bar{\varphi}_{SL} = L_S \bar{i}_{SL} + M \bar{i}_{RL} \tag{16}$$

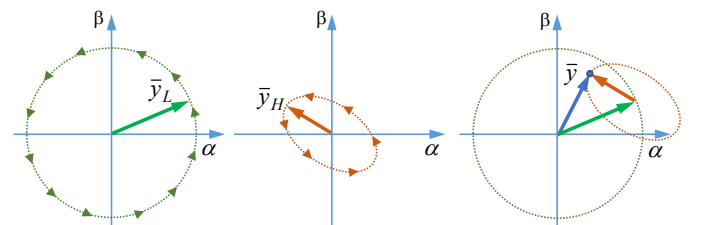$$\bar{\varphi}_{RL} = L_R \bar{i}_{RL} + M \bar{i}_{SL} \tag{17}$$

Fig. 3. Frequency decomposition of a generic variable $\bar{y}$.

$$\bar{v}_{SH} = R_S \, \bar{i}_{SH} + \frac{d\bar{\varphi}_{SH}}{dt} + j\omega\bar{\varphi}_{SH} \qquad (18)$$

$$\bar{v}_{RH} = R_R \, \bar{i}_{RH} + \frac{d\bar{\varphi}_{RH}}{dt} + j(\omega - \omega_m)\bar{\varphi}_{RH} \qquad (19)$$

$$\bar{\varphi}_{SH} = L_S \, \bar{i}_{SH} + M \, \bar{i}_{RH} \qquad (20)$$

$$\bar{\varphi}_{RH} = L_R \, \bar{i}_{RH} + M \, \bar{i}_{SH} \, . \qquad (21)$$

The frequency separation suggests employing the low-frequency components in (14)-(17) for torque control and the high-frequency components in (18)-(21) for power transfer. However, by substituting (8)-(13) in (5)-(6), a cross-coupling effect between the low- and high-frequency components appears in the expressions of torque and rotor power, resulting in torque and power ripple:

$$T = T_L + T_{LH} + T_H \qquad (22)$$

$$P_R = P_{R,L} + P_{R,LH} + P_{R,H}. \qquad (23)$$

In (22)-(23), subscripts L and H indicate terms that depend respectively on low-frequency and high-frequency variables, while the subscript LH indicates the cross-coupling terms. The equations of these components are derived in Sections II.B, II.C, and II.D.

Usually, torque pulsation of the motor is not well tolerated in positioning systems for automated machines. In contrast, the pulsation of P_R results in the fluctuation of E_{DCR}, which can be mitigated by selecting a proper value of C_R. Therefore, the proposed control algorithm aims to suppress the torque ripple generated by the power transfer process.

B. Control of the main torque contribution

The low-frequency components in (14)-(17) can be used to regulate the main torque generated by the machine using a field-oriented control scheme implemented on a d-q reference frame synchronous and aligned with the low-frequency component of the rotor flux vector in (13). Moreover, the rotor inverter can emulate a virtual short circuit of the rotor winding, like in a squirrel cage rotor, by forcing $\bar{v}_{RL}$ equal to zero. Considering the above conditions, (15) and (17) can be rewritten as follows:

$$0 = R_R \, i_{RLd} + \frac{d\varphi_{RLd}}{dt} \qquad (24)$$

$$0 = R_R \, i_{RLq} + (\omega_L - \omega_m)\varphi_{RLd} \qquad (25)$$

$$\varphi_{RLd} = L_R \, i_{RLd} + M \, i_{SLd} \qquad (26)$$

$$0 = L_R \, i_{RLq} + M \, i_{SLq}. \qquad (27)$$

The angular speed ω_L in (25) is the angular frequency of the flux vector $\bar{\varphi}_{RL}$ in the stationary reference frame of the machine.

Replacing (26) in (24) and considering the torque component T_L in (22), one obtains the following pair of equations:

$$\varphi_{RLd} = \frac{M}{1 + \tau_R s} i_{SLd} \qquad (28)$$

$$T_L = \frac{3}{2} p \frac{M}{L_R} \varphi_{RLd} \, i_{SLq} \qquad (29)$$

where $\tau_R = L_R/R_R$ is the time constant of the rotor circuit. Equations (28) and (29) show that the flux component φ_{RLd} depends on the current i_{SLd}, while the torque T_L depends on the magnitude φ_{RLd} of the rotor flux and i_{SLq}. Therefore, to produce

a constant torque component T_L, the d-q components of the current vector $\bar{i}_{SL}$ should be constant at steady state. Moreover, to maximize the torque response of the drive, the magnetizing current i_{SLd} can be kept constant, while the control of the instantaneous value of T_L is left to i_{SLq}. In this condition, (28) and (29) can be expressed in a more compact form:

$$\varphi_{RLd} = M i_{SLd} \qquad (30)$$

$$T_L = \frac{3}{2} p \frac{M^2}{L_R} i_{SLd} i_{SLq}. \qquad (31)$$

C. Control of the power absorbed from the rotor winding.

The method used to decouple the power transfer from the torque production is based on the independent control of the d-axis and q-axis currents. The d-axis current is primarily responsible for power transfer, while q-axis variables are controlled to reduce torque ripple components in (22). For easier understanding, an intuitive separation of the roles of the d-q components of $\bar{i}_{SH}$ and $\bar{i}_{RH}$ is depicted in Fig. 4. The d-q reference frame considered in this analysis is the same one used for the control of the main torque contribution T_L, i.e., aligned with the flux vector $\bar{\varphi}_{RL}$.

The voltage on the DC-link capacitor E_{DCR} shown in Fig.2 can be controlled by the power P_R extracted from the rotor winding of the machine. By recalling that $\bar{v}_{RL} = 0$, the expression of P_R in (23) is as follows:

$$P_R = P_{R,LH} + P_{R,H} = -\frac{3}{2}\bar{v}_{RH} \cdot \bar{i}_{RL} - \frac{3}{2}\bar{v}_{RH} \cdot \bar{i}_{RH}. \qquad (32)$$

The term $P_{R,LH}$ is the dot product of two vectors at different frequencies, which always determines a pulsating power with a zero-mean value. Conversely, the second term $P_{R,H}$ shows a non-zero mean value if vectors $\bar{v}_{RH}$ and $\bar{i}_{RH}$ are not orthogonal. Therefore, the voltage E_{DCR} can be regulated through the average value of the active power extracted from the rotor, which depends only on $P_{R,H}$. In addition, $P_{R,H}$ in (32) can be decomposed into the d and q contributions by expanding the dot product as follows:

$$P_{R,H} = P_{R,Hd} + P_{R,Hq} = -\frac{3}{2}v_{RHd}i_{RHd} - \frac{3}{2}v_{RHq}i_{RHq}. \qquad (33)$$

The proposed control algorithm entrusts the power transfer to the d-axis variables, while the q-axis variables are used to compensate for the torque ripple. Therefore, the power contribution $P_{R,Hq}$ cannot be freely controlled since it depends
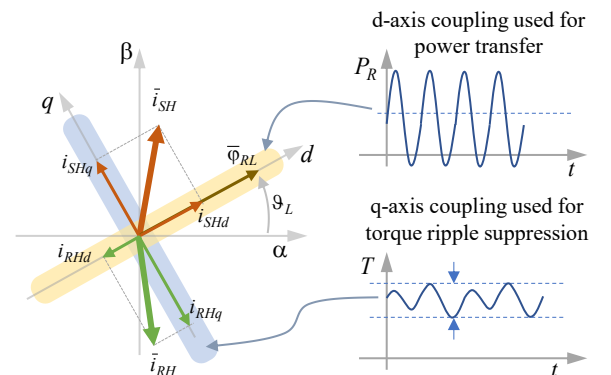
Fig. 4. Separation of the roles of the d-q components of $\bar{i}_{SH}$ and $\bar{i}_{RH}$.

on the torque ripple suppression strategy illustrated in the next Section. Thus, the regulation of the DC-link capacitor E_{DCR} is obtained using the contribution $P_{R,Hd}$.

A viable method to transfer power from stator to rotor by employing only the d-frame variables is to induce a variation of the rotor flux φ_{RHd}. The d component of the voltage vector $\bar{v}_{RH}$ can be derived by (19) as follows:

$$v_{RHd} = R_R i_{RHd} + \frac{d\varphi_{RHd}}{dt} - (\omega_L - \omega_m)\varphi_{RHq} . \quad (34)$$

Equation (34) shows that i_{RHd} is weakly dependent on φ_{RHq} if the derivative of φ_{RHd} is much higher than the motional voltage $(\omega_L - \omega_m)\varphi_{RHq}$. This condition is met if φ_{RHd} is excited by injecting a pulsating current i_{SHd} with constant magnitude I_{SHd} and angular speed ω_H into the stator winding:

$$i_{SHd} = I_{SHd}\sin(\omega_H t). \quad (35)$$

By substituting (21) in (34) and considering (35), one finds:

$$v_{RHd} = R_R i_{RHd} + L_R \frac{di_{RHd}}{dt} + \omega_H M I_{SHd}\cos(\omega_H t) - (\omega_L - \omega_m)\varphi_{RHq} \quad (36)$$

The motional term in (36) can be neglected if the pulsation ω_H is much higher than the angular slip $(\omega_L - \omega_m)$. This condition can be easily obtained because the slip frequency in an induction machine controlled with a field-oriented control scheme is few Herz. Thus, by selecting a proper value for ω_H, (36) becomes independent of the q-axis variables as follows:

$$\omega_H \gg (\omega_L - \omega_m) \Rightarrow v_{RHd} \cong R_R i_{RHd} + L_R \frac{di_{RHd}}{dt} + V_{exc}\cos(\omega_H t). \quad (37)$$

The excitation voltage V_{exc} in (37) is a constant term defined as:

$$V_{exc} = \omega_H M I_{SHd} . \quad (38)$$

A simple way to adjust the power $P_{R,Hd}$ is to emulate a virtual resistance R_{VR} on the d-axis. Thus, the rotor inverter can be controlled to synthetize a voltage v_{RHd} proportional to the current i_{RHd}:

$$v_{RHd} = -R_{VR} i_{RHd} . \quad (39)$$

By substituting (39) in (37), one finds:

$$(R_R + R_{VR}) i_{RHd} + L_R \frac{di_{RHd}}{dt} + V_{exc}\cos(\omega_H t) = 0. \quad (40)$$

It can be easily verified that the steady-state solution of (40) is

$$i_{RHd} = -I_{RHd}\cos(\omega_H t - \gamma_{RHd}), \quad (41)$$

where I_{RHd} and γ_{RHd} are the magnitude and the phase angle of i_{RHd}:

$$I_{RHd} = \frac{V_{exc}}{\sqrt{(R_R + R_{VR})^2 + (\omega_H L_R)^2}} \quad (42)$$

$$\gamma_{RHd} = \tan^{-1}\frac{\omega_H L_R}{R_R + R_{VR}} . \quad (43)$$

The final expression of the power contribution $P_{R,Hd}$ in (33) can be derived considering (41) and (39) as follows:

$$P_{R,Hd} = \hat{P}_{R,Hd}\left[1 + \cos(2\omega_H t - 2\gamma_{RHd})\right]. \quad (44)$$

The average power term $\hat{P}_{R,Hd}$ in (44) is equal to

$$\hat{P}_{RHd} = \frac{3}{4}\frac{R_{VR}V_{exc}^2}{(R_R + R_{VR})^2 + (\omega_H L_R)^2} . \quad (45)$$

Equation (44) shows that the power P_{RHd} comprises a DC contribution and an AC term at frequency $2\omega_H$. Thus, the average power extracted from the rotor can be adjusted by

controlling the virtual resistance R_{VR} imposed by the rotor-side inverter.

D. Suppression of the torque ripple.

The torque generated by the machine is composed of the main contribution T_L and the additional terms T_{LH} and T_H, as shown in (22). It can be verified that at steady state, T_{LH} and T_H are:

$$T_{LH} = \frac{3}{2}p\frac{M}{L_R}\left[(L_R i_{RHd} + M i_{SHd})i_{SLq} - L_R i_{RHq} i_{SLd}\right] \quad (46)$$

$$T_H = \frac{3}{2}pM\left[i_{RHd}i_{SHq} - i_{RHq}i_{SHd}\right]. \quad (47)$$

Equation (46) shows that T_{LH} is a term generated by the interaction between low and high-frequency currents. Since i_{SLd} and i_{SLq} are constant at steady state, T_{LH} is a pulsating AC torque at angular frequency ω_H. Conversely, torque contribution T_H in (47) is generated only by high-frequency current components. Thus, T_H generally contains a DC term and a ripple at angular frequency $2\omega_H$.

Section II.C has demonstrated that the power flow can be controlled by the d-component of the stator and rotor current vectors $\bar{i}_{SH}$ and $\bar{i}_{RH}$. Therefore, the q-components of the currents are degrees of freedom that can be used to suppress the torque ripple in (46) and (47).

The torque pulsation T_{LH} can be zeroed if the term inside the square bracket in (46) is equal to zero. It worth recalling that i_{SLd} and i_{SLq} are related to the main torque contribution T_L generated by the machine, while i_{SHd} and i_{RHd} are used to control the power transfer. Therefore, i_{RHq} is the only independent variable that can be used for zeroing T_{LH}. By setting (46) equal to zero, and solving for i_{RHq}, one finds:

$$i_{RHq} = \frac{L_R i_{RHd} + M i_{SHd}}{L_R}\frac{i_{SLq}}{i_{SLd}}. \quad (48)$$

The current i_{RHq} is a linear combination of the d-components of the stator and rotor high-frequency currents. Moreover, it depends on the ratio between the torque command current i_{SLq} and the magnetizing current i_{SLd}. Current i_{RHq} at steady state can be generally expressed as follows:

$$i_{RHq} = I_{RHq}\sin(\omega_H t - \gamma_{RHq}), \quad (49)$$

where I_{RHq} and γ_{RHq} in (49) are the magnitude and the phase angle of the current. The quantities I_{RHq} and γ_{RHq} can be obtained by substituting (35), (41) and (49) in (48), leading to

$$I_{RHq} = \frac{i_{SLq}}{i_{SLd}}\sqrt{\left(\frac{M}{L_R}I_{SHd}\right)^2 - 2\frac{M}{L_R}I_{SHd}I_{RHd}\sin\gamma_{RHd} + I_{RHd}^2} \quad (50)$$

$$\gamma_{RHq} = \gamma_{RHd} . \quad (51)$$

The last degree of freedom, i_{SHq}, can be used to manipulate the torque contribution T_H. Equation (47) can be expressed in an explicit form by assuming that, at steady state, the current i_{SHq} is as follows:

$$i_{SHq} = I_{SHq}\cos(\omega_H t - \gamma_{SHq}). \quad (52)$$

By substituting (35), (41), (49) and (52) into (47), it can be noted that the torque T_H is composed of a constant term $T_{H,DC}$ and a pulsating contribution $T_{H,AC}$ at angular frequency $2\omega_H$ as follows:
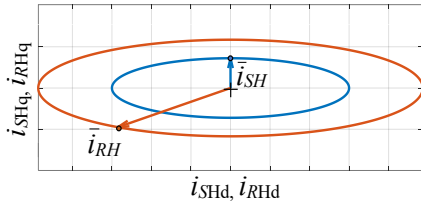
Fig. 5. Typical trajectories followed by the stator and rotor current vectors $\bar{\imath}_{SH}$ and $\bar{\imath}_{RH}$.

$$T_H = T_{H,DC} + T_{H,AC} \tag{53}$$

$$T_{H,DC} = -\frac{3pM}{4}[I_{RHd}I_{SHq}\cos(\gamma_{SHq}-\gamma_{RHd})+I_{RHq}I_{SHd}\cos\gamma_{RHq}] \tag{54}$$

$$T_{H,AC} = \frac{3pM}{4}\big[I_{RHq}I_{SHd}\cos(2\omega_H t-\gamma_{RHq}) \\ - I_{RHd}I_{SHq}\cos(2\omega_H t-\gamma_{RHd}-\gamma_{SHq})\big]. \tag{55}$$

Current i_{SHq} can be shaped to suppress the term $T_{H,AC}$ by selecting I_{SLq} and γ_{SHq} in (53) as follows:

$$I_{SHq} = \frac{I_{RHq}I_{SHd}}{I_{RHd}} \tag{56}$$

$$\gamma_{SHq} = 0. \tag{57}$$

Fig. 5 shows an example of the trajectories followed by $\bar{\imath}_{SH}$ and $\bar{\imath}_{RH}$. The length of the major and minor axes of the ellipses depends on the operating condition of the drive. However, the aspect ratio of the stator and rotor ellipses is always the same. The side effect of the suppression of the AC term $T_{H,AC}$ is the generation of the following constant torque contribution $T_{H,DC}$, which must be compensated by the main torque T_L to control the motion of the drive.

$$T_{H,DC} = -\frac{3pM}{2}I_{RHq}I_{SHd}\cos\gamma_{RHd}. \tag{58}$$

It is worth noting that the torque disturbance depends on $\cos\gamma_{RHd}$, which is negligible if the angle in (43) tends to $\pi/2$. This result can be obtained by selecting a proper value of the frequency ω_H.

III. CONTROL SCHEME

The control scheme of the drive is shown in Fig. 6. The scheme consists of two parts for the control of the stator and rotor inverters. The vectors with superscript "S" and "R" represent quantities respectively in the α-β reference frame of the stator and rotor, whereas the vector quantities without any superscript are defined in the d-q frame, whose d-axis is aligned to the flux vector $\bar{\varphi}_{RL}$. The position of the rotor flux vector is derived using an Indirect Field Oriented Control (IFOC) approach.

The control of the low-frequency d-q components of the stator current is based on a traditional rotor field-oriented control as discussed in Section II.B. The setpoint for i_{SLq} is adjusted by the speed controller (a), while the current i_{SLd} is kept constant at its rated value and produces, at steady state, a rotor flux φ_{R1d} with magnitude Mi_{SLd}. Conversely, the setpoints of the high-frequency d-q components of $\bar{\imath}_{SH}$ are calculated according to (35) and (52). The resulting reference current $\bar{\imath}_{S,ref}$ is tracked by the Proportional-Integral-Resonant (PIR) controllers (b) and (c), which provide the reference stator voltage $\bar{v}_{S,ref}$. The dynamic performance of the current control loop is improved by the feed-forward compensation of the back-electromotive forces, which are added to the output signals of the regulators.

On the rotor side, the DC-link voltage E_{DCR} is regulated by the PI controller (d), which directly adjusts the average power $\hat{P}_{R,Hd}$ extracted from the machine through the virtual resistance $R_{VR,ref}$. In fact, if ω_H is sufficiently high and V_{exc} is constant, the
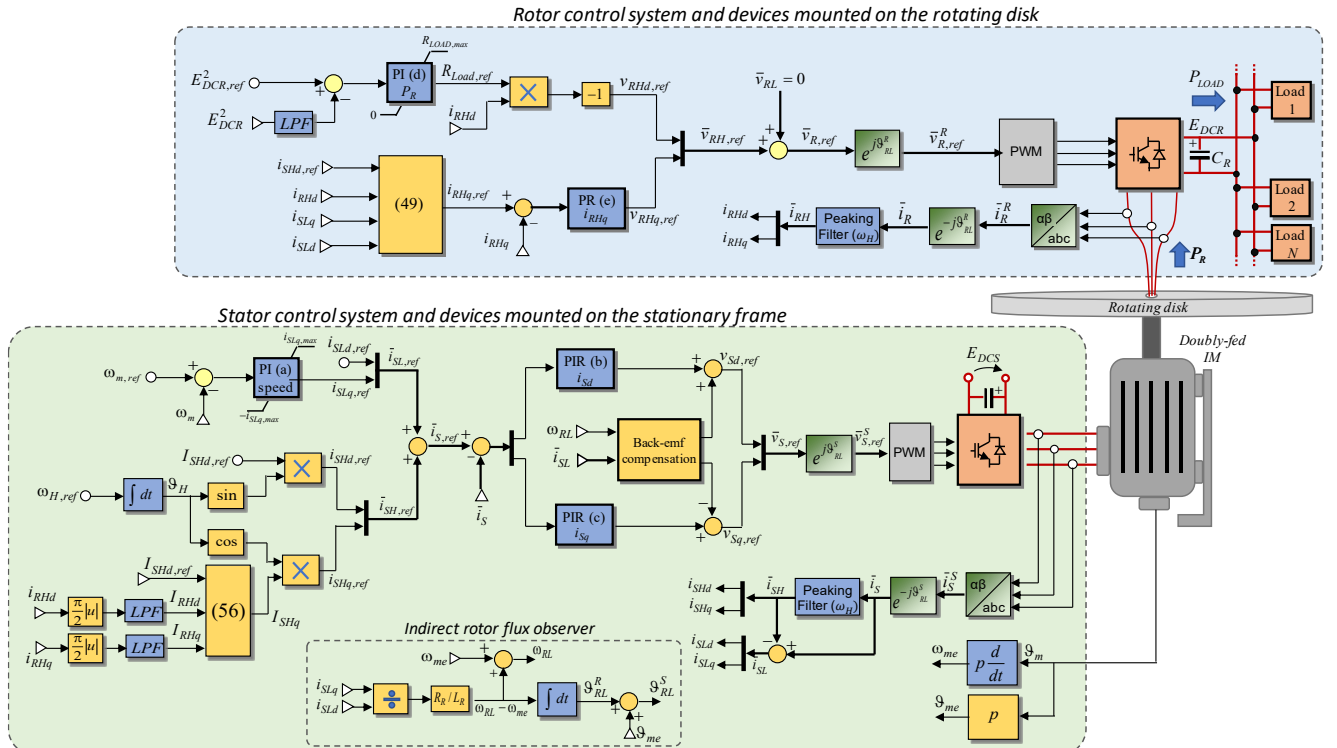

Fig. 6 - Schematic and control scheme of the wound-rotor induction motor drive.

resistive term at the denominator of (45) becomes negligible with respect to $\omega_H L_R$. Thus, the average power $\hat{P}_{R,Hd}$ becomes proportional to R_{VR} as follows:

$$\hat{P}_{RHd} \cong \frac{3}{4} R_{VR} \left(\frac{V_{exc}}{\omega_H L_R} \right)^2 \propto R_{VR} \qquad (59)$$

Once $R_{VR,ref}$ is available, the reference voltage component $v_{RHd,ref}$ can be calculated according to (39). The d-q components of $\bar{i}_{RH}$ are obtained from $\bar{i}_R$ by means of peaking filters tuned at the angular frequency ω_H.

Finally, the control scheme in Fig. 6 shows that the reference value of i_{RHq} is calculated as in (48) to suppress the torque component T_{LH}. The Proportional-Resonant (PR) controller (e) adjusts the voltage $v_{RHq,ref}$ to track the reference value of i_{RHq}. The d-q components of the rotor voltage are then combined to form the total reference voltage vector $\bar{v}_{R,ref}$.

IV. EXPERIMENTAL RESULTS

A complete test setup has been realized to verify the effectiveness of the proposed control technique. The system includes a three-phase wound-rotor four poles induction motor, two three-phase IGBT inverters, a DC power supply and an electronic load, as shown in Fig. 7. The two three-phase inverters are based on 1200 V - 100 A power modules from Infineon (IFS100B12N3E4_B31). To reduce the complexity of the experimental setup, a commercial doubly-fed induction generator for wind energy applications has been adopted, whose electric parameters are listed in Table I. This solution allows accessing the rotor winding from the stationary frame through the slip-rings. Moreover, a DC machine used as a generator has been used to control the braking torque applied to the machine under test.

In the experimental results, the magnetizing current i_{SLd} is kept constant at 6 A, while the current i_{SHd} is a sinusoidal waveform with a constant angular frequency of 50 Hz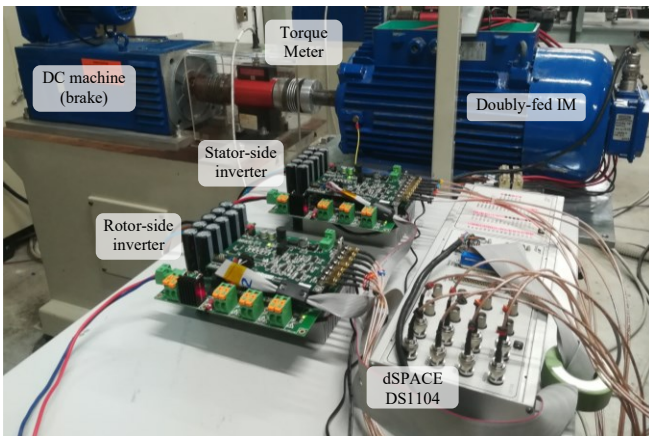. It is worth noting that the reference values for ω_H and I_{Sdh} are related to the maximum power level that can be transferred to the rotor loads. By combining (38) and (45), one finds:

$$\hat{P}_{RHd} = \frac{3}{4} \frac{R_{VR} V_{exc}^2}{(R_R + R_{VR})^2 + (\omega_H L_R)^2} \qquad (60)$$

For a given configuration (ω_H, I_{Sdh}), the power $\hat{P}_{R,Hd}$ depends only on R_{VR}, as shown in Fig. 8.

The virtual resistance R_{VR} that maximizes the function $\hat{P}_{R,Hd}$ can be found by imposing $\frac{\partial \hat{P}_{R,Hd}}{\partial R_{VR}} = 0$ and solving for R_{VR}. It can be shown analytically that the power transfer is maximized when the external resistance R_{VR} equals the rotor side impedance (analogous to the maximum power transfer theorem) as follows:

$$R_{VR,P\max} = \sqrt{R_R^2 + (\omega_H L_R)^2} \;. \qquad (61)$$

By using (60) and (61), the maximum power level for any configuration (ω_H, I_{Sdh}) can be calculated as reported in Fig. 9. The red point in the figure highlights the combination (ω_H, I_{Sdh}) used during the experimental tests. Its selection depends on the following motivations. In rotary assembly stations, the electric loads located on the rotating disk are typically sensors (temperature, position, industrial cameras, etc.), processing units, antennas, and small electrical actuators. Therefore, this paper aims to reach a target level of 100 W. The second constraint in the selection of (ω_H, I_{Sdh}) is due to the limited bandwidth (150 Hz) of the torque meter available in the
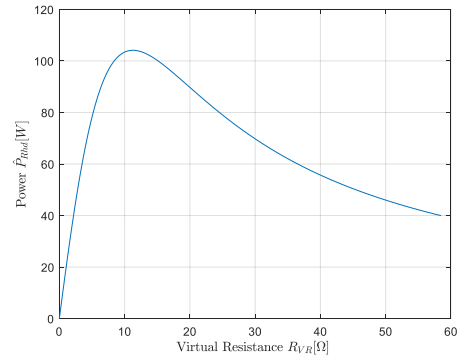
Fig. 8 - Extracted power $\hat{P}_{R,Hd}$ as a function of the virtual resistance considering $\omega_H = 2\pi 50 \; rad/s$ and $I_{Sdh} = 3.5A$.
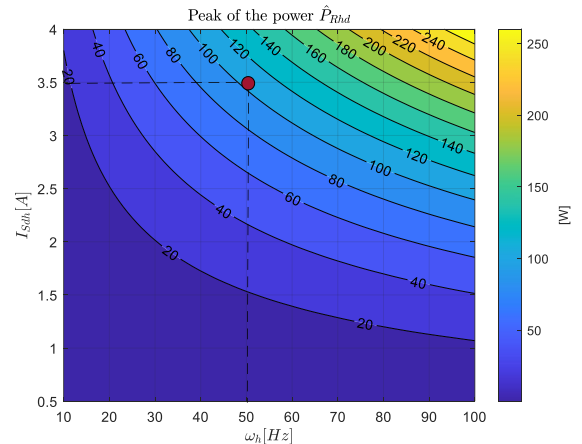
TABLE I
ELECTRIC PARAMETERS OF THE DOUBLY-FED MACHINE

$R_S = 0.53 \; \Omega$	$R_R = 0.31 \; \Omega$
$L_S = 83$ mH	$L_R = 19$ mH
$M = 38$ mH	$p = 2$

Fig. 7 - Picture of the test setup.

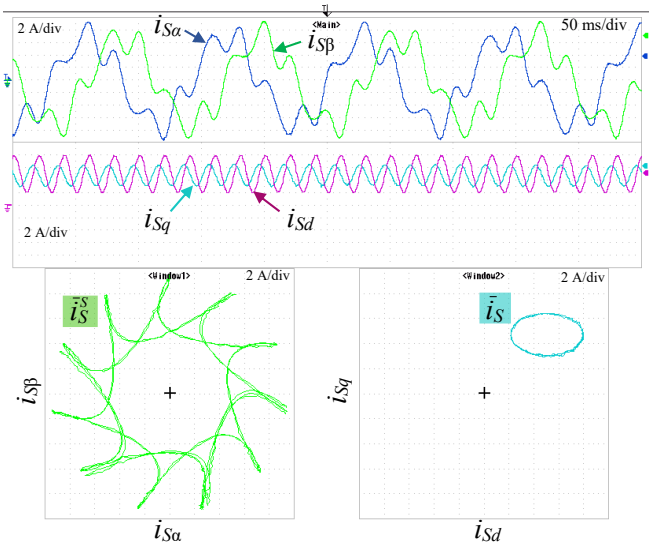Fig. 9 - Peak values of $\hat{P}_{R,Hd}$ as a function of the angular frequency ω_H and the magnitude I_{Sdh}.

Fig. 10 - Waveforms of the α-β and d-q components of the stator currents (2 A/div) at steady state. Trajectories of the currents in the α-β and d-q planes.
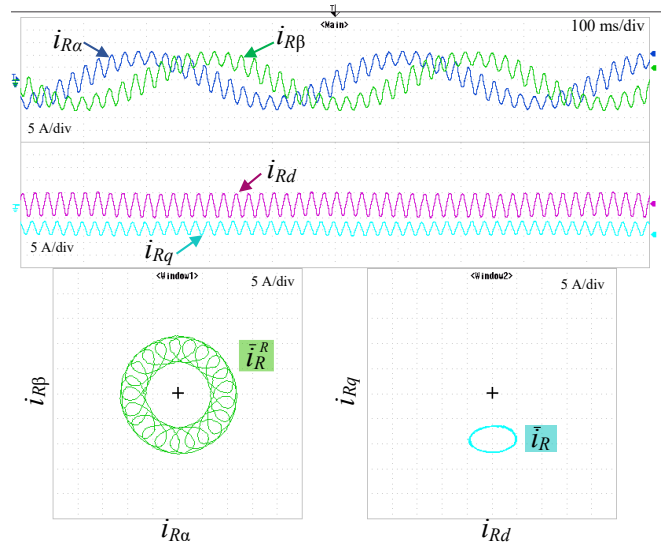

Fig. 11 - Waveforms of the α-β and d-q components of the rotor currents (5 A/div) at steady state. Trajectories of the currents in the α-β and d-q planes.

laboratory (Staiger Mohilo 0160 dm and signal amplifier). Therefore, to reach the target power level and measure the effectiveness of the method in terms of torque ripple reduction, ω_H and I_{Sdh} have been set to $2\pi50\ rad/s$ and 3.5 A respectively.

Fig. 10 and Fig. 11 show the time evolution of the α-β and d-q components of the stator and rotor current vector and their resulting trajectories in the α-β and d-q plane when the motor rotates at a constant angular speed, and constant electric power is transferred to the rotor. As can be seen, i_{Sd} and i_{Sq} comprise a DC term and a sinusoidal contribution at 50 Hz, resulting in an elliptical trajectory with the center at the coordinate $\bar{\iota}_{SL}$. Similarly, $\bar{\iota}_R$ draws an elliptical orbit in the d-q plane with the center at the coordinate $\bar{\iota}_{RL}$. These results prove that the

developed scheme can control the low and high-frequency components of the stator and rotor current vector in the d-q reference frame.

The effectiveness of the torque ripple suppression method illustrated in Section II.D has been verified. Fig. 12 shows the d-q components of $\bar{\iota}_S$ and $\bar{\iota}_R$, and the torque at the shaft when the machine rotates at 200 rpm and transfers an average power of 100 W to the rotor. In the first part of the test, the torque ripple suppression technique is not activated. The zoomed view 1 shows that the currents i_{SHq} and i_{RHq} are zero, and the torque generated by the machine is composed of a DC term of nearly 7 Nm and a peak-to-peak ripple of 2.5 Nm at 50 Hz. At time t_0, the torque ripple suppression control is activated, and the reference values of i_{SHq} and i_{RHq} are calculated as in (56) and
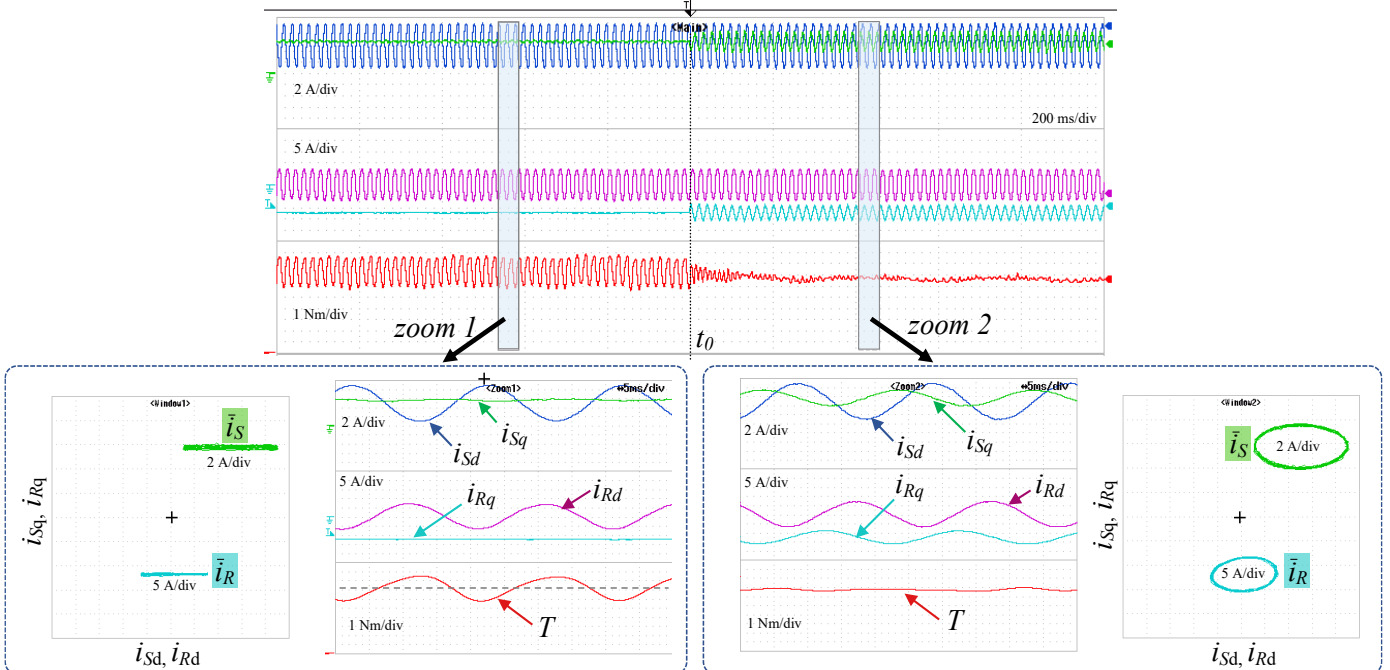

Fig. 12 – Effectiveness of the torque ripple suppression control. Waveforms of the d-q components of the stator currents (2 A/div), rotor currents (5 A/div), and torque T (1 Nm/div).
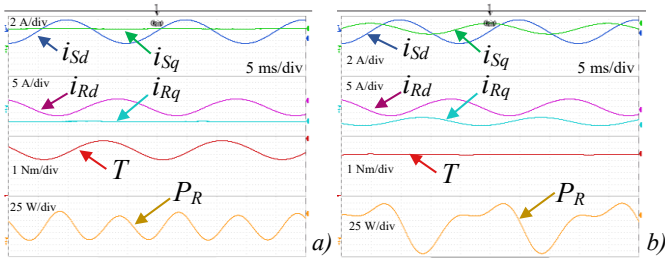
Fig. 13 - Effect of the torque ripple suppression control on the rotor power. Waveforms of the d-q components of the stator currents (2 A/div), rotor currents (5 A/div), torque T (1 Nm/div) and rotor power P_R (25 W/div).
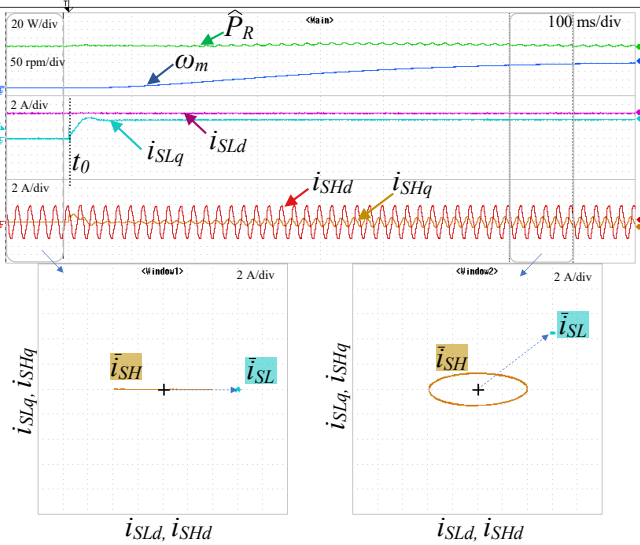

Fig. 14 - Behavior of the drive during a speed transient from zero to 150 rpm while the power delivered to the rotor loads is 100 W. Waveforms of the rotor power P_R (20 W/div), mechanical speed (50 rpm/div), d-q components of low- and high-frequency stator currents (2 A/div) and their respective trajectories in the d-q plane.

(48). It can be clearly noted in the zoomed view 2 that the torque ripple greatly reduces.

Section II.A and II.C point out that the torque ripple generated by the power transfer can be suppressed to the detriment of pulsation of the power P_R. This theoretical aspect is reported in Fig. 13 (a) and (b). The figure shows the steady state waveforms of the d-q components of $\bar{\imath}_S$ and $\bar{\imath}_R$, the motor torque, and the power P_R when the torque ripple suppression algorithm is respectively disabled and enabled. It can be noted that the rotor power P_R in Fig. 13 (a) is formed by a DC component and an AC term at $2\omega_H$. In fact, in this condition, P_R corresponds to the term $P_{R,Hd}$ in (44). It can be verified that, if i_{SHq} and i_{RHq} are zero, the expression (32) becomes equal to (44), leading to $P_R = P_{R,Hd}$. Conversely, if i_{SHq} and i_{RHq} are non-zero, as in Fig. 13(b), the power expression also includes a disturbance term in DC and at angular speed ω_H. The controller of the rotor DC-link voltage compensates the disturbance terms by adjusting the power $\hat{P}_{R,Hd}$ through the virtual resistance R_{VR}, so that the average value of E_{DCR} is regulated at its rated value.

Fig. 14 illustrates the behavior of the drive during a speed transient from zero to 150 rpm while the power delivered to the rotor loads is 100 W. The figure shows the waveforms of the average rotor power, the mechanical speed, and the decomposition of the stator current vector in the low-frequency
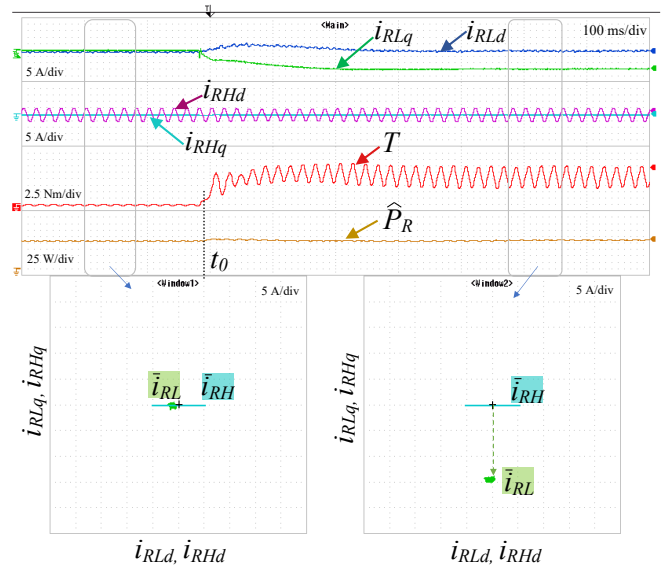

Fig. 15 – Locked rotor behavior of the drive during a step change of the torque command while the power delivered to the rotor loads is 100 W and the torque ripple suppression scheme is not activated. Waveforms of the torque T (2.5 Nm/div) and average rotor power $\hat{P}_R$ (25 W/div) d-q components of the low- and high-frequency rotor currents (5 A/div) and their respective trajectories in the d-q plane.
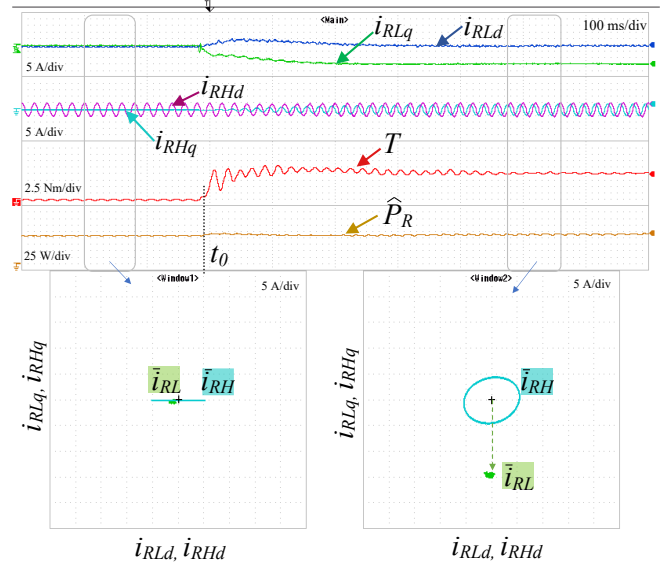

Fig. 16 - Locked rotor behavior of the drive during a step change of the torque command while the power delivered to the rotor loads is 100 W and the torque ripple suppression scheme is activated. Waveforms of the torque T (2.5 Nm/div) and average rotor power $\hat{P}_R$ (25 W/div) d-q components of the low- and high-frequency rotor currents (5 A/div) and their respective trajectories in the d-q plane.

and high-frequency contributions $\bar{\imath}_{SL}$ and $\bar{\imath}_{SH}$. At time t_0, a step variation of the current i_{SLq} accelerates the rotor up to 150 rpm. During the speed transient, the average power $\hat{P}_R$ is finely regulated at 100 W by the control system of the rotor inverter. It can also be noted that i_{SHq} depends on the operating condition of the drive. A particular case shown in the figure is when the rotor is at standstill, and the torque current i_{SLq} equals zero. In this condition, i_{RHq} and i_{SHq} are zero owing to (48) and (56).

The effectiveness of the torque suppression algorithm with the rotor at standstill is analyzed in Figs. 15 and 16. The figures show the waveforms of the average rotor power, the shaft
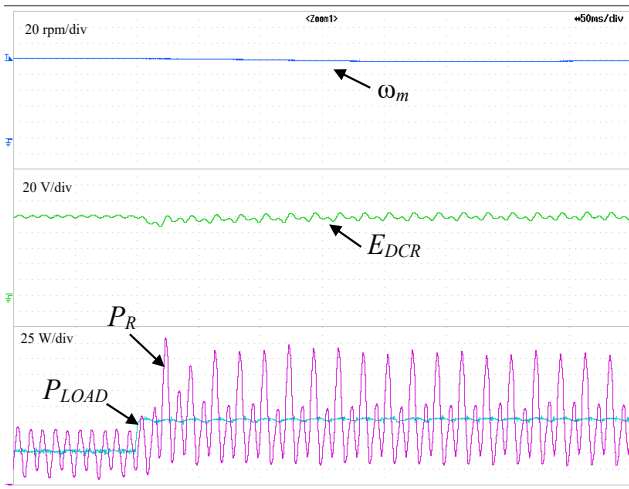
Fig. 17 - Behavior of the system during a variation of the rotor power while the machine rotates at a constant speed. From top to bottom: ω_m (20 rpm/div), E_{DCR} (20 V/div), P_R (25 W/div), and P_{LOAD} (25 W/div).

Fig. 18 - Emulation of a generic working cycle for rotary assembly stations. From top to bottom: ω_m (20 rpm/div), E_{DCR} (20 V/div), $\hat{P}_R$ (20 W/div), and P_{LOAD} (20 W/div).

torque, and the decomposition of the rotor current vector into the contributions $\bar{\imath}_{RL}$ and $\bar{\imath}_{RH}$. Before time t_0, the shaft torque is zero and the average rotor power is 100 W. Thus, the control algorithm can transfer power to the rotor side even when both torque and speed are zero. At time t_0, a step of i_{SLq} is imposed, resulting in a negative current i_{RLq} and generating nearly 10 Nm at the shaft. During this torque transient, the system regulates the rotor current i_{RHd} to maintain the rotor power at 100 W. The effectiveness of the torque ripple suppression algorithm can be noted by comparing the torque waveforms reported in the two figures. In Fig. 15, the currents i_{SHq} and i_{RHq} are set to zero, as considered in [22], resulting in a relevant torque ripple. Conversely, Fig. 16 shows a significant reduction in torque ripple after controlling i_{SHq} and i_{RHq} in accordance with (56) and (48).

The response of the speed and power control loops to a sudden change in the power absorbed by the rotor loads is illustrated in Figure 17. During the test, the mechanical speed is set to 100 rpm, and the setpoint of E_{DCR} is 100 V. It can be noted that the AC terms of the rotor power are absorbed by the capacitor C_R, resulting in the fluctuation of the voltage E_{DCR}. The DC-link capacitance has been selected to 560 µF to make the voltage ripple negligible.

Finally, the behavior of the drive system during a working cycle for a rotary assembly station was emulated by setting the speed and rotor load power profiles. The test results, consisting of the mechanical speed, the rotor inverter DC voltage E_{DCR}, the load power P_{LOAD}, and the average power extracted from the rotor winding $\hat{P}_R$ are reported in Fig. 18. The drive follows a periodic trapezoidal speed profile, which starts from zero and peaks at 100 rpm. At the same time, the electronic rotor load is programmed to absorb a base power of 20 W, followed by peaks of 100 W in order to mimic the power profile of a periodic machining process. It can be observed that the motion and the power transfer can be controlled simultaneously at any rotor speed and power level.

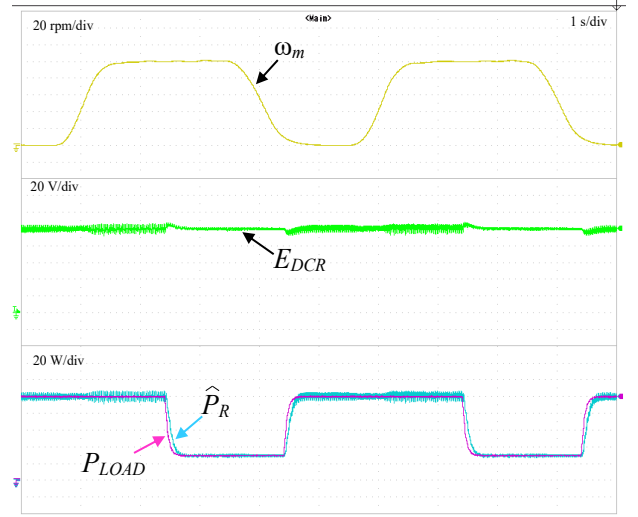The experimental results reported in this Section confirm that the proposed control scheme can independently regulate the speed of the machine, the power transferred to the rotor loads, and suppress the torque ripple as expected.

V. CONCLUSION

The paper investigates the use of a gearless doubly-fed three-phase induction machine in automation applications based on rotary assembly stations. The drive aims to independently control the motion of the platform and the power transferred to the actuators and sensors located on the rotating disk. Torque control is achieved by injecting low-frequency current components into the machine windings, while high-frequency currents are used for WPT. However, a cross-coupling effect between the low and high-frequency components generally leads to torque and power pulsation. The control scheme proposed in this paper, which is extensively analyzed in Section II, allows the suppression of the torque ripple. The experimental results confirm the feasibility of the integrated drive and the effectiveness of the control scheme.

ACKNOWLEDGMENT

REFERENCES

[1] K. Sawa, Y. Watanabe, and T. Ueno, "Effect of lubricant on sliding conditions in Au-plated slip-ring system for small electric power transfer," in IEEE Holm Conference on Electrical Contacts (Holm), New Orleans, LA, 2014, pp. 1-6.

[2] J. K. SkjØlberg, H. F. Ohma, and M. Runde, "Wear rates and current distribution of carbon brushes on steel slip rings," *IEEE Trans. Energy Convers.*, vol. 24, no. 4, pp. 835-840, Dec. 2009.

[3] H. Ma, T. Chen, Y. Zhang, P. Ju, and Z. Chen, "Research on the fault diagnosis method for slip ring device in doubly-fed induction generators

based on vibration," *IET Renew. Power Gener.*, vol. 11, no. 2, pp. 289-295, 2017.

[4]   R. D. Hall and R. P. Roberge, "Carbon brush performance on slip rings," in Conference Record of Annual Pulp & Paper Industry Technical Conference, San Antonio, TX, 2010, pp. 1-6.

[5]   S. Zhao et al., "Study of carbon brush and slip-ring system abrasion from electric contact friction under special environments," *IEEE Access*, vol. 9, pp. 9308-9317, 2021.

[6]   Y. Zhang, J. Yang, D. Jiang, D. Li and R. Qu, "Design, manufacture, and test of a rotary transformer for contactless power transfer system," *IEEE Trans. on Magn.,* vol. 58, no. 2, pp. 1-6, Feb. 2022.

[7]   X. Zhu, B. Lin, L. Liu and Y. Luan, "Power transfer performance and cutting force effects of contactless energy transfer system for rotary ultrasonic grinding," *IEEE Trans. Ind. Electron.*, vol. 63, no. 5, pp. 2785-2795, May 2016.

[8]   K. D. Papastergiou and D. E. Macpherson, "An airborne radar power supply with contactless transfer of energy - part I: rotating transformer," *IEEE Trans. Ind. Electron.*, vol. 54, no. 5, pp. 2874-2884, Oct. 2007.

[9]   D. Bortis, L. Fässler, A. Looser and J. W. Kolar, "Analysis of rotary transformer concepts for high-speed applications," in Annual IEEE Applied Power Electronics Conference and Exposition (APEC), Long Beach, CA, USA, 2013, pp. 3262-3269.

[10] H. Zhong, L. Zhao and X. Li, "Design and analysis of a three-phase rotary transformer for doubly fed induction Generators," *IEEE Trans. Ind. Appl.*, vol. 51, no. 4, pp. 2791-2796, July-Aug. 2015.

[11] R. Manko, S. Čorović and D. Miljavec, "Analysis and design of rotary transformer for wireless power transmission," in IEEE Problems of Automated Electrodrive. Theory and Practice (PAEP), 2020, pp. 1-6.

[12] J. Dai, S. Hagen, D. C. Ludois, I. P. Brown, "Synchronous generator brushless field excitation and voltage regulation via capacitive coupling through journal bearings," *IEEE Trans. Ind. Appl.*, vol. 53, no. 4, pp. 3317-3326, July-Aug. 2017.

[13] J. Dai, D. C. Ludois, "A Survey of wireless power transfer and a critical comparison of inductive and capacitive coupling for small gap applications," *IEEE Trans. Power Electron.*, vol. 30, no. 11, pp. 6017-6029, Nov. 2015.

[14] A. S. Khalik, M. I. Masoud, B. W. Williams, A. L. Mohamadein, and M. M. Ahmed, "Steady-state performance and stability analysis of mixed pole machines with electromechanical torque and rotor electric power to a shaft-mounted electrical load," *IEEE Trans. Ind. Electron.*, vol. 57, no. 1, pp. 22-34, Jan. 2010.

[15] A. R. Munoz and T. A. Lipo, "Dual stator winding induction machine drive," *IEEE Trans. Ind. Appl.*, vol. 36, no. 5, pp. 1369-1379, Sept.-Oct. 2000.

[16] G. Rizzoli, M. Mengoni, A. Tani, G. Serra, L. Zarri, D. Casadei, "Wireless power transfer using a five-phase wound-rotor induction machine for speed-controlled rotary platforms," *IEEE Trans. Ind. Electron.*, Vol. 67, No. 8, pp. 6237-6247, Aug. 2020.

[17] G. Rizzoli, M. Mengoni, G. Sala, L. Vancini, L. Zarri, A. Tani, R. Bojoi, "Exploitation of the power capability in a five-phase doubly fed induction motor drive for contact-less energy transfer," *IEEE Trans. Ind. Electron.*, vol. 69, no. 8, pp. 7596-7606, Aug. 2022.

[18] V. Yaramasu, B. Wu, P. C. Sen, S. Kouro and M. Narimani, "High-power wind energy conversion systems: state-of-the-art and emerging technologies," in Proceedings of the IEEE, vol. 103, no. 5, pp. 740-788, May 2015.

[19] R. Cardenas, R. Pena, S. Alepuz and G. Asher, "Overview of control systems for the operation of DFIGs in wind energy applications," *IEEE Trans. Ind. Electron.*, vol. 60, no. 7, pp. 2776-2798, July 2013.

[20] A. Tapia, G. Tapia, J. X. Ostolaza and J. R. Saenz, "Modeling and control of a wind turbine driven doubly fed induction generator," *IEEE Trans. Energy Convers.*, vol. 18, no. 2, pp. 194-204, June 2003.

[21] Y. Han, S. Kim, J. I. Ha, and W. J. Lee, "A doubly fed induction generator controlled in single-sided grid connection for wind turbines," *IEEE Trans. Energy Convers.*, vol. 28, no. 2, pp. 413-424, June 2013.

[22] M. Mengoni, G. Rizzoli, L. Zarri, A. Tani, A. Amerise and G. Serra, "Control of a three-phase wound-rotor induction motor drive for automation applications," in IEEE International Electric Machines & Drives Conference (IEMDC), San Diego, CA, USA, 2019, pp. 1267-1272.

[23] G. Rizzoli, M. Mengoni, G. Sala, L. Zarri, and A. Tani, "Torque pulsation reduction in three-phase doubly fed induction machine for wireless energy transfer applications," in IEEE Energy Conversion Congress and Exposition (ECCE), 2021, pp. 4921-4926.

Gabriele Rizzoli received the M.Sc and Ph.D. degree in Electrical Engineering, respectively, in 2012 and 2016, from the University of Bologna, Bologna, Italy. He is currently a Junior Assistant Professor at the Department of Electrical, Electronic and Information Engineering "G. Marconi" of the University of Bologna. His research interests include the design of electrical machines, the development and control of high-efficient power converters for automotive and renewable energy applications.

Michele Mengoni received the M.Sc. (with honors) and Ph.D. degrees in electrical engineering from the University of Bologna, Bologna, Italy, in 2006 and 2010, respectively. He is currently an Associate Professor with the Department of Electrical, Electronic and Information Engineering "G. Marconi," University of Bologna. His research interests include the design, analysis, and control of three phase electric machines, multiphase drives, and ac/ac matrix converters. Currently, he serves as an Associate Editor for IEEE Trans. on Industrial Electronics.
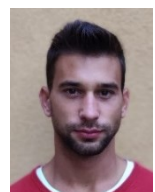
Luca Vancini received the M.Sc. and Ph.D. degree in Electrical Engineering from the University of Bologna, Bologna, Italy, in 2018 and 2022, respectively. Currently, he is a Research Fellow with the Department of Electrical, Electronic and Information Engineering "G. Marconi," University of Bologna. His research interests include power electronics, control of multiphase converters and diagnostic techniques for multiphase machines.

Giacomo Sala (Member, IEEE) received the B.Sc. degree in power engineering, the M.Sc. (hons.) degree in electrical engineering, and the Ph.D. in electrical machines and drives from the University of Bologna, Bologna, Italy, in 2012, 2014, and 2018, respectively. Until 2019, he was a Researcher with the Power Electronics, Machines and Control Group, Department of Electrical and Electronic Engineering, The University of Nottingham, Nottingham, U.K. Since 2019, he has been a Researcher with the Department of Electrical, Electronic, and Information Engineering "Guglielmo Marconi," University of Bologna, where he has been a Junior Assistant Professor, since 2020. His research interests include the design, modeling, and control of multiphase electrical machines, fault-tolerant control, and fault diagnosis of electric drives.

Luca Zarri received the M. Sc. and Ph.D. degrees in Electrical Engineering from the University of Bologna, Bologna, Italy, in 1998 and 2007, respectively. Currently, he is a Full Professor of power electronics, electrical machines and drives with the Department of Electrical, Electronic, and Information Engineering "Guglielmo Marconi" of the University of Bologna. He has authored or co-authored more than 170 scientific papers. His research activity concerns the control of power converters and electric drives. He is a senior member of the IEEE Industry Applications, IEEE Power Electronics and IEEE Industrial Electronics Societies. Currently, he is the Chair of the IEEE IAS Industrial Drives Committee.

Angelo Tani received the M. Sc. degree in Electrical Engineering, with honors, from the University of Bologna, Bologna, Italy, in 1988. Currently he is a Full Professor of power electronics, electrical machines and drives with the Department of Electrical, Electronic and Information Engineering "Guglielmo Marconi," University of Bologna. He has authored more than 200 papers published in technical journals and conference proceedings. His current activities include modeling, control, and fault diagnosis of multiphase electric machines.